Geophysical Research Letters

RESEARCH LETTER
10.1029/2019GL082915

Geodynamo Conductivity Limits

Peter E. Driscoll[1] **and Zhixue Du**[2,3]

[1]Department of Terrestrial Magnetism, Carnegie Institution for Science, Washington, DC, USA, [2]Geophysical Laboratory, Carnegie Institution for Science, Washington, DC, USA, [3]State Key Laboratory of Isotope Geochemistry, Guangzhou Institute of Geochemistry, Chinese Academy of Sciences, Guangzhou, China

Key Points:
- Planetary magnetic field generation is predicted to peak as a function of electrical and thermal conductivity
- Electrical conductivity limits of thermal dynamo action are derived in terms of material properties and core temperature
- Geodynamo regime diagram shows that the geomagnetic field approached shutdown prior to inner core nucleation

Supporting Information:
- Supporting Information S1

Correspondence to:
P. E. Driscoll,
pdriscoll@ciw.edu

Citation:
Driscoll, P. E., & Du, Z. (2019). Geodynamo conductivity limits. *Geophysical Research Letters*, *46*. https://doi.org/10.1029/2019GL082915

Received 22 MAR 2019
Accepted 2 JUL 2019
Accepted article online 8 JUL 2019

Abstract In a metal, as in Earth's core, the thermal and electrical conductivities are assumed to be correlated. In a planetary dynamo this implies a contradiction: that both electrical conductivity, which makes it easier to induce current and magnetic field, and conductive heat transport, which hinders thermal convection, should increase simultaneously. Here we show that this contradiction implies that the magnetic induction rate peaks at a particular value of electrical and thermal conductivity and derive the low- and high-conductivity limits for thermal dynamo action. A dynamo regime diagram is derived as a function of electrical conductivity and temperature for Earth's core that identifies four distinct dynamo regimes: no dynamo, thermal dynamo, compositional dynamo, and thermocompositional dynamo. Estimates for the temperature-dependent electrical conductivity of the core imply that the geodynamo may have come close to its high-conductivity "no dynamo" limit prior to inner core nucleation, consistent with recent paleomagnetic observations.

1. Introduction

Planetary dynamos are maintained by inducing magnetic fields through fluid motions faster than they decay by magnetic diffusion. Convection in a metallic core is typically driven by either thermal cooling, where the heat removed from the core exceeds the amount that can be conducted in the absence of motion, or by compositional buoyancy, where a phase change generates a gravitationally unstable density anomaly. Such processes must be common given the evidence for dynamos in the iron-rich cores of most rocky planets in the solar system. Three of the four terrestrial planets plus the Moon and Ganymede all have an active dynamo today or evidence of one in their past (Schubert & Soderlund, 2011), with Venus being the possible lone exception. The fact that most rocky planets have or had internally generated magnetic fields implies that dynamo action in iron cores is relatively common, particularly in young planets, and that it is perhaps more difficult to maintain over billions of years.

Recent upward revisions to the thermal and electrical conductivity of high-pressure and high-temperature iron (Davies et al., 2015; de Koker et al., 2012; Gomi et al., 2016; Konôpková et al., 2016; Ohta et al., 2016; Pozzo et al., 2012; Seagle et al., 2013; Silber et al., 2018; Wagle et al., 2018; Xu et al., 2018) have renewed interest in how Earth has maintained a dynamo over 3.5–4 Ga. The modern geodynamo is thought to be driven primarily by the release of light elements at the inner core boundary associated with the solidification of the inner core. Although the age of the inner core is unknown, it is likely younger than the oldest paleomagnetic evidence, implying that some other mechanism must have been driving the ancient geomagnetic field (Olson, 2013). The two favored options are a thermal dynamo driven by a superadiabatic core-mantle boundary (CMB) heat flux (e.g., Driscoll & Bercovici, 2014; Davies et al., 2015; Nimmo, 2015), or an exsolution dynamo driven by the separation of a chemically saturated species from the core like MgO or SiO_2 (e.g., Hirose et al., 2017; O'Rourke & Stevenson, 2016). Both of these plausible solutions depend strongly on the value of the core thermal and electrical conductivities.

A simple and reliable way to characterize the operation of a dynamo is to compute its magnetic Reynolds number (Rm), the ratio of magnetic induction to magnetic diffusion. We develop a simple model for estimating Rm associated with thermal convection as a function of core temperature and electrical conductivity. We then apply the model to the Earth by estimating the CMB heat flux and energy available to drive dynamo action. Finally, we compare our derived electrical conductivity limit to thermal dynamo action to an

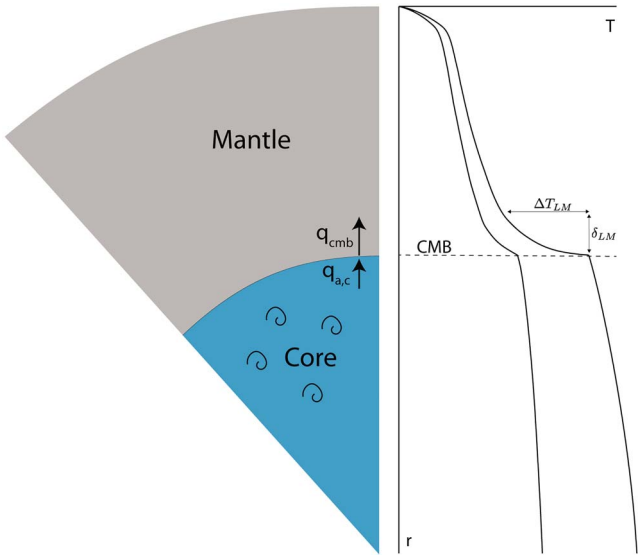

Figure 1. Schematic of a planetary interior showing the solid mantle and underlying liquid core. Example temperature profiles (right) encompass the lower mantle thermal boundary layer above the CMB and an adiabatic profile below at two different CMB temperatures. CMB = core-mantle boundary.

empirical estimate of the temperature-dependent core electrical conductivity and explore whether the geodynamo is expected to have operated continuously throughout Earth history.

2. Theory

In its simplest form a dynamo can be described by the ratio of magnetic induction ($\boldsymbol{\nabla} \times (\mathbf{u} \times \mathbf{B})$) to diffusion ($\eta \nabla^2 \mathbf{B}$), known as the magnetic Reynolds number (Rm)

$$Rm = \mu_0 \sigma u D \tag{1}$$

where μ_0 is magnetic permeability, σ is electrical conductivity, u is convective fluid velocity, $\eta = 1/\mu_0\sigma$ is magnetic diffusivity, and D is a characteristic length scale (e.g., Roberts, 2015). Laboratory and numerical studies systems with $Rm > 40$ are generally found to be supercritical for dynamo action (Christensen & Aubert, 2006; Monchaux et al., 2009).

Recent revisions to the conductivity of iron prompts the question: What does (1) predict for systems at very high or low electrical conductivity? At first glance (1) implies that dynamo action would be more likely in systems with high σ and that Rm, and thereby the magnetic field, will grow with σ. For example, dynamo action would be expected to be easier in a liquid metal than in a liquid silicate. But this assumes a comparable convective velocity. Does fluid velocity depend on electrical conductivity? If so how?

In a metal, like in Earth's core, electrons are assumed to dominate the conductive transport of electric charge and heat, implying that the thermal and electrical conductivities are correlated, known as the Wiedmann-Franz law:

$$k = \sigma L T \tag{2}$$

where $L = 2.44 \times 10^{-8}$ WΩK^{-2} is the ideal Lorenz number (e.g., Pourovskii et al., 2017) and T is temperature. Therefore, higher electrical conductivity implies higher thermal conductivity, which means there is less heat available to drive convection at a given cooling rate. Together, (1) and (2) imply a contradiction for dynamo action: as electrical conductivity increases, making magnetic induction more efficient, the thermal conductivity should increase, decreasing the convective heat flux and velocity u, making induction less efficient. So does magnetic induction grow with σ or not? How does Rm depend on σ? Is there an "optimal" σ for dynamo action?

To answer these questions we explore below how Rm depends on σ, and, in particular, what determines the convective velocity u in (1) and how it can depend on σ. We will then apply this model to Earth's core and discuss the implications.

2.1. Convection Model

To investigate the energetics of a planetary core we consider a two-layer planet with a silicate mantle overlying a metallic core that is a rotating and electrically conductive fluid shell (or sphere) of thickness D undergoing Rayleigh-Bernard convection (Figure 1). The mantle is assumed to be less efficient at transporting heat, thereby determining the core cooling rate and electrically insulating. We aim to derive an expression for Rm in (1) that is a function of σ and T_{cmb} (CMB temperature) that identifies the conductivity limits of dynamo action. Previously, Rm conditions have been derived that describe bounds on the growth rate of the magnetic field (e.g., Roberts, 2015), but they do not account for the global energetics or thermal conductivity of the system.

First, we relate the convective velocity u in (1) to the energy available to drive convection via scaling laws developed by a range of numerical and experimental fluid dynamical studies (e.g., Aurnou et al., 2015; Christensen & Aubert, 2006; Olson & Christensen, 2006). To derive an expression for fluid velocity u we use the dimensionless convective fluid velocity, or Rossby number (Ro),

$$Ro \equiv \frac{u}{\Omega D} = Ro_0 Ra_Q^{\alpha} \tag{3}$$

where Ω is angular rotation rate, and the right-hand side is a scaling law where Ro_0 is a coefficient of order one, α depends on the assumed force balance, and Ra_Q is a reduced Rayleigh number related to the available convective energy (Olson & Christensen, 2006). The predicted values of $\alpha = 2/5$ derived from a balance of Coriolis, inertial, and buoyancy forces (Aubert et al., 2001) or $\alpha = 4/9$ from a balance of Coriolis, Lorentz, and buoyancy forces (Davidson, 2013) bracket the range found in rotating convection simulations of $\alpha \approx 0.41$ in Boussinesq systems (Christensen & Aubert, 2006) and $\alpha \approx 0.45$ in anelastic systems (Yadav et al., 2013). Acknowledging that there is a range of possible values, we adopt the nominal values from Christensen and Aubert (2006) of $Ro_0 = 0.85$ and $\alpha = 2/5$. A comparison of $\alpha = 2/5$ to $\alpha = 4/9$ shows that the scaled Rm values differ by ~7% (see supporting information).

Solving for u in (3)

$$u = Ro_0 \Omega D Ra_Q^{\alpha} \quad . \tag{4}$$

The reduced Rayleigh number Ra_Q is (and see supporting information; Aubert et al., 2009)

$$Ra_Q = \frac{r_o^2 F}{D^4 \Omega^3} \tag{5}$$

where $D = r_o - r_i$, r_o and r_i are the radii of the outer and inner boundaries, and F is buoyancy flux. The buoyancy flux F is in general a sum of thermal and compositional sources. For simplicity we initially consider a purely thermal buoyancy $F = F_T$ so that Rm is a thermal magnetic Reynolds number, with

$$F_T = \frac{\alpha_{T,c} g_c q'}{\rho_c c_c} \tag{6}$$

where convective heat flux q',

$$q' = q_{\text{cmb}} - q_{a,c} \tag{7}$$

is the difference between the CMB heat flux

$$q_{\text{cmb}} = k_{\text{LM}} \frac{\mathrm{d}T}{\mathrm{d}r} \approx k_{\text{LM}} \frac{\Delta T_{\text{LM}}}{\delta_{\text{LM}}} \tag{8}$$

and the adiabatic heat flux required to keep the top of the core isentropic,

$$q_{a,c} = k_c \frac{\mathrm{d}T_a}{\mathrm{d}r} = k_c \gamma_{a,c} T_{\text{cmb}} \quad . \tag{9}$$

In the above $\alpha_{T,c}$ is core thermal expansivity, g_c is gravity, ρ_c is core density, c_c is core specific heat, k_{LM} and k_c are the lower mantle and core thermal conductivities, $\Delta T_{\text{LM}} = T_{\text{cmb}} - T_{\text{LM}}$ is temperature drop across the lower mantle boundary layer of thickness δ_{LM}, and $\gamma_{a,c} = g\alpha_{T,c}/c_c$ is the inverse of the core adiabatic scale height. $q' > 0$ implies thermal convection while $q' < 0$ implies thermal stratification.

2.2. Lower Mantle Thermal Boundary Layer

There are several possible approaches to estimating the thermal boundary layer heat flux q_{cmb} in (8) (e.g., Sotin & Labrosse, 1999). The critical thermal boundary layer model has been found to be as accurate as parameterized convection and mixing-length theory in predicting the lower boundary layer heat flow in convection in a spherical shell (Tachinami et al., 2011). Here we adopt the critical thermal boundary layer model from Driscoll and Bercovici (2014) because it relies only on local boundary layer properties, limiting the number of assumptions required (see section S2 in the supporting information). To compute the lower mantle thermal boundary layer thickness δ_{LM} in (8) we adopt an Arrhenius law for lower mantle viscosity ν_{LM} (see section S2 in the supporting information).

At this point there are two unknown temperatures: T_{LM} at the top of the lower mantle thermal boundary layer and T_{cmb} at the CMB. These temperatures can be related by assuming the mantle and core secular cooling rates are equal, which implies

$$\Delta T_{\text{LM}} = T_{\text{cmb}}(1 - \Gamma) + T_{\text{cmb},0}\Gamma - T_{\text{LM},0} \tag{10}$$

where $\Gamma = \frac{M_c c_c}{M_m c_m} \approx 0.275$ is the ratio of core to mantle heat capacity, M_m and M_c are mantle and core mass, c_m and c_c are mantle and core specific heat, and $T_{\text{cmb},0}$ and $T_{\text{LM},0}$ are the initial CMB and lower mantle temperatures (see section S2). $T_{\text{LM},0}$ is computed from (10) for assumed present-day temperatures $T^*_{\text{cmb}} = 4{,}000$ K and $T^*_{\text{LM}} = 2{,}500$ K and an arbitrary initial core temperature $T_{\text{cmb},0}$. We have also assumed the thermal boundary layers cool at the same rate as the mantle or core so that $\dot{T}_m \approx \dot{T}_{\text{LM}}$ and $\dot{T}_c \approx \dot{T}_{\text{cmb}}$.

2.3. Conductivity Limits

The thermal magnetic Reynolds number Rm in (1) can now be rewritten by combining (1)–(10) to give

$$Rm = Rm_0 T_{\mathrm{cmb}}^{2\alpha} \sigma^{1+\alpha} \left(\frac{\sigma_{crit}}{\sigma} - 1 \right)^{\alpha} \tag{11}$$

where the constant coefficient Rm_0 is

$$Rm_0 = \mu_0 Ro_0 r_o^{2\alpha} \Omega^{1-3\alpha} D^{2(1-2\alpha)} \left[\frac{\alpha_{T,c} g_c L \gamma_{a,c}}{\rho_c c_c} \right]^{\alpha} \tag{12}$$

which has a value of $Rm_0 \approx 5.09 \times 10^{-8}$ K$^{-4/5}(\Omega\mathrm{m})^{7/5}$ for Earth's present-day core and $\alpha = 2/5$ (a detailed derivation and general form of (11) are in the supporting information). From (11) it can be seen that Rm has two roots: $\sigma = \sigma_1 = 0$ and $\sigma = \sigma_2 = \sigma_{\mathrm{crit}}$, where the "critical conductivity" is

$$\sigma_{\mathrm{crit}} = \frac{q_{\mathrm{cmb}}}{L \gamma_{a,c} T_{\mathrm{cmb}}^2} = \frac{k_{\mathrm{LM}}^{2/3}}{L \gamma_{a,c}} \left(\frac{\alpha_{T,\mathrm{LM}} g_{\mathrm{LM}} \rho_{\mathrm{LM}} c_m}{Ra_{\mathrm{crit}}} \right)^{1/3} \frac{\Delta T_{\mathrm{LM}}^{4/3}}{\nu_{\mathrm{LM}}^{1/3} T_{\mathrm{cmb}}^2} \tag{13}$$

with units of conductivity (parameter values are in Table S1 in the supporting information). The root $\sigma_1 = 0$ describes a hypothetical system that conducts no electricity and, therefore, also cannot support a dynamo. The root $\sigma_2 = \sigma_{\mathrm{crit}}$ in (13) corresponds to the case where $q_{\mathrm{cmb}} = q_{a,c}$, which implies that the core is neutrally stable ($q' = 0$) and no pure thermal convection is possible.

Similarly, a set of critical conductivities for thermal dynamo action can be derived by setting $Rm = Rm_D \approx 40$ and solving for σ_D, giving

$$\sigma_{D1} = \frac{Rm_D}{Rm_0} \frac{1}{T_{\mathrm{cmb}}^{2\alpha} \sigma_{\mathrm{crit}}^{\alpha}} \tag{14}$$

at the lower limit, and

$$\sigma_{D2} = \frac{\sigma_{\mathrm{crit}}}{1 + \frac{\sigma_{D1}}{\sigma_{\mathrm{crit}}}} \tag{15}$$

at the upper limit (see supporting information for details). The latter expression may be further simplified by noting that typically $\sigma_{D1}/\sigma_{\mathrm{crit}} \ll 1$ giving

$$\sigma_{D2} \approx \sigma_{\mathrm{crit}} \quad . \tag{16}$$

Consequently, the conductivities σ_{D1} and σ_{D2} are lower and upper conductivity limits to a thermally driven dynamo. It can also be shown from (11) that a peak in Rm occurs at

$$\sigma_3 = \left[1 - \frac{1}{1 + 1/\alpha} \right] \sigma_{\mathrm{crit}} \approx 0.71 \sigma_{\mathrm{crit}} \tag{17}$$

for $\alpha = 2/5$ (see supporting information for details).

In equation (13) σ_{crit} is inversely proportional to the Lorentz number L. It has been proposed that the Lorentz number may differ from its ideal value L_0 at high pressure (Konôpková et al., 2016; Pourovskii et al., 2017; Secco, 2017), which can be accounted for by a substitution of $L = cL_0$ in (13), where the constant coefficient c accounts for the nonideality. For example, adopting the reduction of L proposed by Pourovskii et al. (2017) of $c = 1/1.54$ will increase σ_{crit} by a factor of 1.54 and make thermal dynamo action slightly easier.

3. Application to Earth's Core

Next, we apply this model to Earth's core for a range of plausible CMB temperatures T_{cmb} and derive the electrical conductivity limits to thermal dynamo action. For nominal present-day values of $T_{\mathrm{cmb}}^* = 4{,}000$ K and $\sigma^* = 1 \times 10^6\ \Omega^{-1} \cdot \mathrm{m}^{-1}$ the core adiabatic heat flow from (9) is $Q_{a,c}^* = 12$ TW. This value of $Q_{a,c}^*$ is similar to Nimmo (2015) and about 20% lower than the estimates of Davies et al. (2015) and Labrosse (2015) of $Q_{a,c}^* = 15$ TW, because our assumed adiabatic gradient ($\mathrm{d}T_a/\mathrm{d}r = -\alpha_{T,c} g_{\mathrm{cmb}} T_{\mathrm{cmb}}^*/c_c \approx -0.8$ K/km) is about 20% lower than theirs (−1 K/km). The difference between these gradients reflects uncertainty in $\alpha_{T,c}$, c_c, and T_{cmb}^*. We assume that the present-day CMB heat flow Q_{cmb}^* is equal to $Q_{a,c}^*$, implying that the present-day core is neutrally stable for thermal convection and that compositional convection is driving the present-day geodynamo.

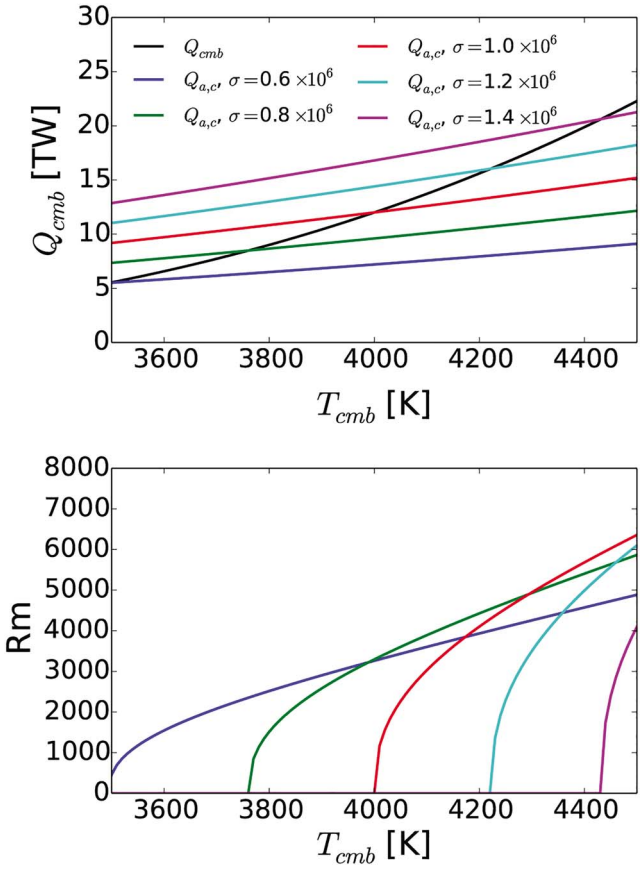

Figure 2. (top) CMB heat flow Q_{cmb} (black) and adiabatic core heat flow $Q_{a,c}$ (colors) as function of T_{cmb} (see legend). $Q_{a,c}$ is computed for a range of electrical conductivities $\sigma = 0.6\text{–}1.4 \times 10^6 \Omega^{-1} \cdot \mathrm{m}^{-1}$ (see legend). (bottom) Thermal magnetic Reynolds number Rm from (11) for the same values of σ in (Figure 2, top). CMB = core-mantle boundary.

Figure 2(top) compares CMB heat flow $Q_{\mathrm{cmb}} = A_{\mathrm{cmb}} q_{\mathrm{cmb}}$ over a range of T_{cmb} to the adiabatic heat flow $Q_{a,c} = A_{\mathrm{cmb}} q_{a,c}$ for a plausible range of σ. Thermal convection is expected when $Q_{\mathrm{cmb}} > Q_{a,c}$, which occurs over all T_{cmb} when σ is low ($0.6 \times 10^6\ \Omega^{-1} \cdot \mathrm{m}^{-1}$) and only occurs at the highest T_{cmb} when σ is high ($1.4 \times 10^6\ \Omega^{-1} \cdot \mathrm{m}^{-1}$) (Figure 2). The thermal magnetic Reynolds number Rm from (11) goes to zero when $Q_{\mathrm{cmb}} = Q_{a,c}$ (i.e., where Q_{cmb} and $Q_{a,c}$ intersect in Figure 2, top), which occurs at higher T_{cmb} for higher σ (Figure 2, bottom). This implies that higher electrical conductivities require larger Q_{cmb} to maintain a thermal dynamo, as expected.

Figure 3 shows Rm in (11) as a function of σ for several choices of T_{cmb}. As expected there is a peak in Rm at intermediate conductivities followed by a precipitous drop as σ approaches σ_{crit} (Figure 3). Estimates of modern Earth-like Rm of 500–2,000 (Christensen et al., 2010) are about a factor of 2 below the peak Rm at $T^*_{\mathrm{cmb}} = 4000$ K, implying that the modern geodynamo does not operate near its peak electrical conductivity. By assumption a nominal present-day value of $\sigma^* = 1 \times 10^6 \Omega^{-1} \cdot \mathrm{m}^{-1}$ at $T^*_{\mathrm{cmb}} = 4000$ K gives a thermal magnetic Reynolds number of zero, leaving compositional convection as the main driving mechanism. Numerical dynamos have shown that a Rm larger than the Earth-like range produce less dipolar fields, while smaller values tend to produce more dipolar fields compared to the geodynamo (Christensen et al., 2010), implying that dynamos that operate near their peak σ may not be dipolar.

Finally, the solutions in Figures 2 and 3 are combined into a $\sigma - T$ phase diagram in Figure 4. For a present-day CMB heat flow of $Q^*_{\mathrm{cmb}} = 12$ TW the upper limit conductivity for thermal dynamo action of $\sigma_{D2}(T_{\mathrm{cmb}}) = \sigma_{\mathrm{crit}}$ from (15) delineates the boundary below which thermal dynamos are possible and above which they are not. Compositional convection is expected as the inner core solidifies, which occurs when $T_{\mathrm{cmb}} < T_{\mathrm{icn}}$ and the core is cooling, where we assume $T_{\mathrm{icn}} \approx 4100$ K is the CMB temperature when the inner core nucleates at the center of the Earth (vertical boundary in Figure 4). Therefore, to the left of this boundary, compositionally driven dynamos are expected.

Together the thermal and compositional driving mechanisms delineate four dynamo regions (see Figure 4 and Table 1): top right, where "no dynamo" occurs because the core is thermally stratified ($\sigma > \sigma_{\mathrm{crit}}$) and fully liquid ($T_{\mathrm{cmb}} > T_{\mathrm{icn}}$); bottom right, where a purely thermal dynamo occurs ($\sigma < \sigma_{\mathrm{crit}}$, $T_{\mathrm{cmb}} > T_{\mathrm{icn}}$); top left, where compositional convection associated with inner core solidification overcomes thermal stratification to drive a purely compositional dynamo ($\sigma > \sigma_{\mathrm{crit}}$, $T_{\mathrm{cmb}} < T_{\mathrm{icn}}$); and bottom left, where both thermal and compositional convection occur, driving a thermochemical dynamo ($\sigma < \sigma_{\mathrm{crit}}$, $T_{\mathrm{cmb}} < T_{\mathrm{icn}}$). Figure 4 also shows how σ_{crit}, that is, the boundary between "no dynamo" and a thermal dynamo, depends on the assumed present-day CMB heat flow Q^*_{cmb}. If Q^*_{cmb} is less than 12 TW, then ν_r increases, σ_{crit} decreases by (13), and the thermal dynamo region shrinks in Figure 4. Conversely, a larger value of Q^*_{cmb} expands the thermal dynamo region.

For the nominal case ($Q^*_{\mathrm{cmb}} = 12$ TW) an empirical estimate for the temperature-dependence of core electrical conductivity σ_T from Ohta et al. (2016) (black curve in Figure 4, also see section S6 in the supporting information) implies that, as the core has cooled, the geodynamo has transitioned from a purely thermal dynamo ($T_{\mathrm{cmb}} > T_{\mathrm{icn}}$) to a thermochemical dynamo ($T_{\mathrm{cmb}} < T_{\mathrm{icn}}$) and eventually to a purely compositional dynamo around $T_{\mathrm{cmb}} = 4000$ K. The present-day core (yellow star in Figure 4) is near $\sigma_{\mathrm{crit}} = 1 \times 10^6\ \Omega^{-1} \cdot \mathrm{m}^{-1}$ at $T_{\mathrm{cmb}} = 4000$ K because we have assumed that the present-day CMB heat flow is equal to the adiabatic value. If instead $Q^*_{\mathrm{cmb}} = 10$ TW, then the geodynamo is predicted to have crossed into the "no dynamo" regime around $T_{\mathrm{cmb}} = 4150$ K, before the inner core nucleated; a scenario highlighted by Olson (2013). Similarly, the core would pass through the "no dynamo" regime prior to inner core nucleation with

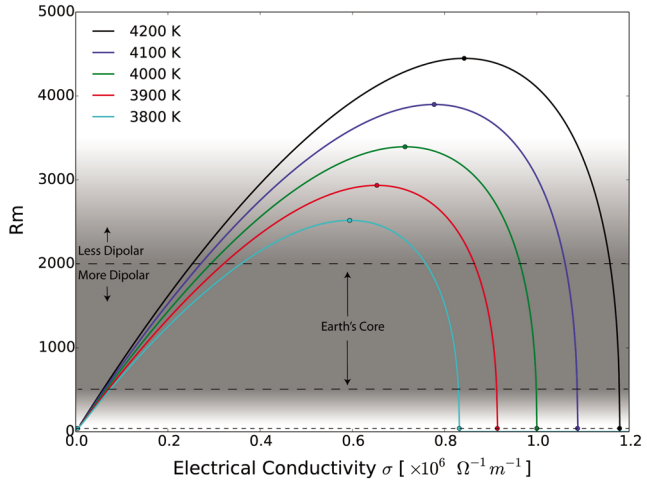

Figure 3. Traces of thermal magnetic Reynolds number $Rm(\sigma)$ for several core-mantle boundary (CMB) temperatures $T_{\rm cmb}$ (see legend) from equation (11). Filled circles correspond to Rm at the critical dynamo conductivities σ_{D1} and σ_{D2}, and peak $Rm(\sigma_3)$. The dark gray region indicates the range of Rm expected for a modern Earth-like dynamo (Christensen et al., 2010). Rm above (below) this range is expected to produce less (more) dipolar magnetic fields (Christensen et al., 2010).

$Q^*_{\rm cmb} = 12$ TW if σ_T is about 20% higher. Recent estimates of σ_T by Xu et al. (2018) are about 20% lower than Ohta et al. (2016) and imply that thermal convection operated continuously prior to inner core nucleation.

Above we assumed that inner core solidification powers a compositional dynamo when $T_{\rm cmb} < T_{\rm icn}$, which is an oversimplification. To address this we estimate the thermal and compositional buoyancy fluxes, F_T and F_χ, at the CMB following the model of Driscoll and Bercovici (2014) and using $Q_{\rm cmb}(T_{\rm cmb})$ from (8). For the nominal values $\sigma = 1\times10^6 \Omega^{-1}\cdot$ m^{-1} and $T_{\rm cmb} = 4000$ K we find that compositional buoyancy $F_\chi = 9.9\times10^{-12}$ m^2/s^3 can overcome thermal stratification $F_T = -2.64\times10^{-16}$ m^2/s^3 to drive a compositional dynamo (where negative buoyancy flux implies stratification). However, compositional convection can be inhibited if thermal stratification is severe enough, which may occur, for example, if the thermal conductivity is too high or compositional buoyancy is too weak. For an extreme case with $T_{\rm cmb} = 3550$ K, where the core is nearly entirely solid, and using a nominal electrical conductivity of $\sigma = 1\times10^6 \Omega^{-1}\cdot$ m^{-1}, we find the compositional buoyancy flux $F_\chi = 2.62\times10^{-12}$ m^2/s^3 is still large enough to overcome the thermal stratification $F_T = -4.09\times10^{-13}$ m^2/s^3. Neutral buoyancy at $T_{\rm cmb} = 3550$ K occurs for $\sigma = 2.95\times10^6 \Omega^{-1}\cdot$ m^{-1}, which is the limiting electrical conductivity for a compositional dynamo at these parameters and exceeds the expected range of σ_T. This should be a lower bound on the limiting conductivity, because at higher $T_{\rm cmb}$ and $Q_{\rm cmb}$ the inner core is expected to grow faster so that compositional buoyancy is stronger, and the thermal and compositional buoyancy flux balance at even higher electrical conductivities (above the range in Figure 4). Therefore, it is safe to assume that a compositional dynamo will occur when $T_{\rm cmb} < T_{\rm icn}$ even if the core is thermally subadiabatic. This analysis applies only at the CMB, but the buoyancy sources and material properties are expected to be functions of depth so that even when the core is stratified at the CMB, convection may occur deeper (Labrosse, 2015).

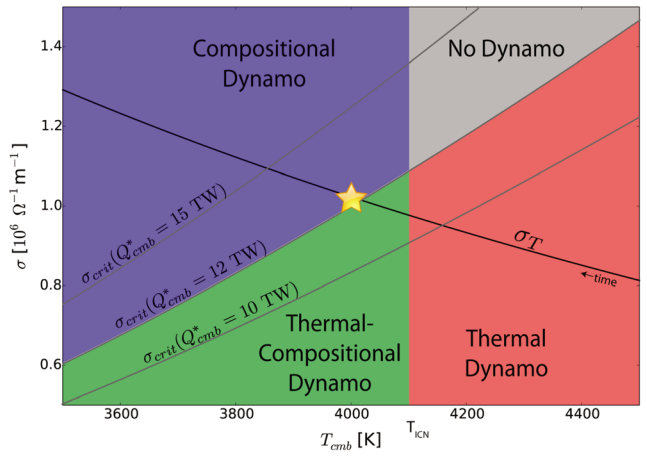

Figure 4. Geodynamo regime diagram: core electrical conductivity σ versus core-mantle boundary (CMB) temperature $T_{\rm cmb}$. An experimental estimate of temperature-dependent electrical conductivity σ_T (black line) from Ohta et al. (2016) (see supporting information) intersects the critical electrical conductivity $\sigma_{D2} = \sigma_{\rm crit}$ (gray lines) from (13) around the present-day $T^*_{\rm cmb}$ (star) assuming $Q^*_{\rm cmb} = 12$ TW. Curves of σ_{crit} (gray lines) denote the upper boundary for purely thermal convection and dynamo action, and is also shown for $Q^*_{\rm cmb} = 10$ and 15 TW. Inner core nucleation at a CMB temperature of $T_{icn} \approx 4100$ denotes the boundary between thermal and compositional convection and dynamo action.

Another important assumption of our model is that thermal cooling and inner core growth are the only driving forces. Alternative mechanisms to thermal and compositional convection have been proposed for Earth's core, including the exsolution of a light species (e.g., Badro et al., 2016; Du et al., 2017; Hirose et al., 2017; O'Rourke & Stevenson, 2016) or tidally forced flows (e.g., Cébron & Hollerbach, 2014; Le Bars et al., 2015). In the case of exsolution, the buoyancy source would be similar to compositional convection associated with inner core solidification as it would occur over a temperature range, and the exsolution rate would depend on the core cooling rate. Therefore, depending on the solubility and initial concentration of the exsolving material, this mechanism has the potential to drive a dynamo in the "no dynamo" region in Figure 4. Du et al. (2017) and Badro et al. (2018) found exsolution of MgO in Earth's core to be possible, but it does not produce sufficient heat to replace radiogenic decay in the thermal budget of the core (Du et al., 2017), which is needed to resolve both the cooling of the mantle and the driving of the core dynamo (Driscoll & Bercovici, 2014). Tidal forcing could potentially drive core flows but they are predicted to prefer thermally stratified regions (Cebron et al., 2010); so it remains unclear whether they can power a dynamo (e.g., Cébron et al., 2019).

4. Implications

In metallic regions of planetary interiors where the thermal and electrical conductivity are related (e.g., via the Wiedemann-Franz Law), a high

Table 1
Four Dynamo Regimes Based on Figure 4

Dynamo regime	$T_{cmb} < T_{icn}$	$T_{cmb} > T_{icn}$
$\sigma > \sigma_{crit}$	Compositional	None
$\sigma < \sigma_{crit}$	Thermal-Compositional	Thermal

thermal and electrical conductivity can have both positive and negative effects on dynamo action. A fluid with low electrical conductivity will produce currents too weak to generate strong magnetic fields, which is one of the main limitations to generating self-sustaining dynamos in the laboratory. However, fluids with very high thermal conductivity can be so efficient at conducting heat that convection is inhibited or stopped entirely, thereby prohibiting dynamo action. These are considered low- and high-conductivity-limited dynamos and are quantified in terms of their magnetic Reynolds number in a simple two-layer planet model. Together these limits imply a maximum *Rm* at intermediate thermal and electrical conductivities. Using nominal values our model predicts that the core has evolved from a purely thermal dynamo to a thermochemical dynamo, avoiding the high conductivity "no dynamo" limit prior to inner core nucleation (Figure 4). This empirical electrical conductivity "path" avoids the "new core paradox" by maintaining a relatively low conductivity in a hot core. However, the uncertainties of several important quantities are large enough to allow a range of outcomes and permit paths that do cross the "no dynamo" region. These uncertainties include the CMB heat flow, the electrical conductivity itself (e.g., Ohta et al., 2016; Xu et al., 2018), the validity of the Wiedemann-Franz law and value of the Lorenz number at high pressure (e.g., Pourovskii et al., 2017; Secco, 2017; Williams, 2018), and the material properties and heat transfer rate of the lower mantle. Among the variables that would make continuous dynamo action more likely include a large present-day CMB heat flow, a low core thermal conductivity, a Lorenz number below the ideal value, a strong inverse dependence of electrical conductivity on temperature, and a hotter inner core nucleation temperature. Interestingly, a path where Earth's core conductivity comes close to, but does not cross, the "no dynamo" region may be consistent with recent suggestions that the geodynamo lingered in a weak-field state prior to inner core nucleation (Driscoll, 2016; Bono et al., 2019).

In summary, we have derived a dynamo regime diagram in $\sigma - T$ space that demonstrates the influence of electrical conductivity on the geodynamo and quantified four dynamo regime boundaries. This regime diagram could be used, for example, to interpret the implications of revisions to relevant material properties or the cooling rate of the core. Analogous dynamo regimes and conductivity limits could be considered in other planetary or astrophysical bodies that display some correlation between their thermal and electrical conductivities, such as other rocky or gaseous planets or the interiors of stars.

Acknowledgments
We thank the Editor and two anonymous reviewers for their constructive comments. The script used to create the plots is available at https://github.com/peteredriscoll/dynamo-limits#dynamo-limits, github/dynamo-limits.

References

Aubert, J., Brito, D., Nataf, H.-C., Cardin, P., & Masson, J.-P. (2001). A systematic experimental study of rapidly rotating spherical convection in water and liquid gallium. *Physics of the Earth and Planetary Interiors*, *128*(1), 51–74. dynamics and Magnetic Fields of the Earth's and Planetary Interiors.

Aubert, J., Labrosse, S., & Poitou, C. (2009). Modeling the paleo-evolution of the geodynamo. *Geophysical Journal International*, *179*(3), 1414–1428. https://doi.org/10.1111/j.1365--246X.2009.04361.x

Aurnou, J., Calkins, M., Cheng, J., Julien, K., King, E., Nieves, D., et al. (2015). Rotating convective turbulence in Earth and planetary cores. *Physics of the Earth and Planetary Interiors*, *246*, 52–71. http://doi.org/10.1016/j.pepi.2015.07.001

Badro, J., Aubert, J., Hirose, K., Nomura, R., Blanchard, I., Borensztajn, S., & Siebert, J. (2018). Magnesium partitioning between Earth's mantle and core and its potential to drive an early exsolution geodynamo. *Geophysical Research Letters*, *45*, 13,240–13,248. https://doi.org/10.1029/2018GL080405

Badro, J., Siebert, J., & Nimmo, F. (2016). An early geodynamo driven by exsolution of mantle components from Earths core. *Nature*, *536*, 326. https://doi.org/10.1038/nature18594

Bono, R. K., Tarduno, J. A., Nimmo, F., & Cottrell, R. D. (2019). Young inner core inferred from Ediacaran ultra-low geomagnetic field intensity. *Nature Geoscience*, *12*(2), 143–147. https://doi.org/10.1038/s41561-018-0288-0

Cébron, D., & Hollerbach, R. (2014). Tidally driven dynamos in a rotating sphere. *The Astrophysical Journal Letters*, *789*(1), L25. https://doi.org/10.1088/2041-8205/789/1/L25

Cébron, D., Laguerre, R., Noir, J., & Schaeffer, N. (2019). Precessing spherical shells: flows, dissipation, dynamo and the lunar core. *Geophysical Journal International*. https://doi.org/10.1093/gji/ggz037

Cebron, D., Maubert, P., & Le Bars, M. (2010). Tidal instability in a rotating and differentially heated ellipsoidal shell. *Geophysical Journal International*, *182*(3), 1311–1318.

Christensen, U., & Aubert, J. (2006). Scaling properties of convection-driven dynamos in rotating spherical shells and application to planetary magnetic fields. *Geophysical Journal International*, *166*(1), 97–114. https://doi.org/10.1111/j.1365--246X.2006.03009.x

Christensen, U., Aubert, J., & Hulot, G. (2010). Conditions for Earth-like geodynamo models. *Earth and Planetary Science Letters*, *296*, 487–496. https://doi.org/10.1016/j.epsl.2010.06.009

Davidson, P. A. (2013). Scaling laws for planetary dynamos. *Geophysical Journal International*, *195*(1), 67–74. https://doi.org/10.1093/gji/ggt167

Davies, C., Pozzo, M., Gubbins, D., & Alfè, D. (2015). Constraints from material properties on the dynamics and evolution of Earth's core. *Nature Geoscience*, *8*(9), 678–685. https://doi.org/10.1038/ngeo2492

de Koker, N., Steinle-Neumann, G., & Vlček, V. (2012). Electrical resistivity and thermal conductivity of liquid Fe alloys at high *P* and *T*, and heat flux in Earth's core. *Proceedings of the National Academy of Sciences*, *109*(11), 4070–4073. https://doi.org/10.1073/pnas.1111841109

Driscoll, P. E. (2016). Simulating 2 Ga of geodynamo history. *Geophysical Research Letters*, *43*, 5680–5687. https://doi.org/10.1002/2016GL068858

Driscoll, P., & Bercovici, D. (2014). On the thermal and magnetic histories of Earth and Venus: Influences of melting, radioactivity, and conductivity. *Physics of the Earth and Planetary Interiors*, *236*, 36–51. https://doi.org/10.1016/j.pepi.2014.08.004

Du, Z., Jackson, C., Bennett, N., Driscoll, P., Deng, J., Lee, K. K., et al. (2017). Insufficient energy from MgO exsolution to power early geodynamo. *Geophysical Research Letters*, *44*, 11,376–11,381. https://doi.org/10.1002/2017GL075283

Gomi, H., Hirose, K., Akai, H., & Fei, Y. (2016). Electrical resistivity of substitutionally disordered hcp Fe–Si and Fe–Ni alloys: Chemically-induced resistivity saturation in the Earth's core. *Earth and Planetary Science Letters*, *451*, 51–61. https://doi.org/10.1016/j.epsl.2016.07.011

Hirose, K., Morard, G., Sinmyo, R., Umemoto, K., Hernlund, J., Helffrich, G., & Labrosse, S. (2017). Crystallization of silicon dioxide and compositional evolution of the Earths core. *Nature*, *543*, 99. https://doi.org/10.1038/nature21367

Konôpková, Z., McWilliams, R. S., Gómez-Pérez, N., & Goncharov, A. F. (2016). Direct measurement of thermal conductivity in solid iron at planetary core conditions. *Nature*, *534*, 99–101. https://doi.org/10.1038/nature18009

Labrosse, S. (2015). Thermal evolution of the core with a high thermal conductivity. *Physics of the Earth and Planetary Interiors*, *247*, 36–55. https://doi.org/10.1016/j.pepi.2015.02.002

Le Bars, M., Cébron, D., & Le Gal, P. (2015). Flows driven by libration, precession, and tides. *Annual review of fluid mechanics*, *47*, 163–193. https://doi.org/10.1146/annurev-fluid-010814-014556

Monchaux, R., Berhanu, M., Aumaître, S., Chiffaudel, A., Daviaud, F., Dubrulle, B., et al. Bourgoin, M., Odier, P., Pinton, J.-F., Plihon, N., & Romain, V.(2009). The von Kármán sodium experiment: Turbulent dynamical dynamos. *Physics of Fluids*, *21*(3), 35108.

Nimmo, F. (2015). Energetics of the Core. In G. Schubert (Ed.), *Treatise on Geophysics, second edition* (pp. 27–55). Oxford: Elsevier.

O'Rourke, J. G., & Stevenson, D. J. (2016). Powering Earth's dynamo with magnesium precipitation from the core. *Nature*, *529*, 387–389. https://doi.org/10.1038/nature16495

Ohta, K., Kuwayama, Y., Hirose, K., Shimizu, K., & Ohishi, Y. (2016). Experimental determination of the electrical resistivity of iron at Earths core conditions. *Nature*, *534*, 95–98.

Olson, P. (2013). The new core paradox. *Science*, *342*, 431–432. https://doi.org/10.1126/science.1243477

Olson, P., & Christensen, U. (2006). Dipole moment scaling for convection-driven planetary dynamos. *Earth Planet Science Letters*, *250*(3-4), 561–571. https://doi.org/10.1016/j.epsl.2006.08.008

Pourovskii, L. V., Mravlje, J., Georges, A., Simak, S. I., & Abrikosov, I. A. (2017). Electron–electron scattering and thermal conductivity of epsilon-iron at Earth's core conditions. *New Journal of Physics*, *19*, 73022.

Pozzo, M., Davies, C., Gubbins, D., & Alfè, D. (2012). Thermal and electrical conductivity of iron at Earth's core conditions. *Nature*, *485*, 355–358. https://doi.org/10.1038/nature11031

Roberts, P. (2015). Theory of the geodynamo. *Treatise on Geophysics*, *8*(3), 57–90.

Schubert, G., & Soderlund, K. (2011). Planetary magnetic fields: Observations and models. *Physics of the Earth and Planetary Interiors*, *187*(3), 92–108. https://doi.org/10.1016/j.pepi.2011.05.013

Seagle, C. T., Cottrell, E., Fei, Y., Hummer, D. R., & Prakapenka, V. B. (2013). Electrical and thermal transport properties of iron and iron-silicon alloy at high pressure. *Geophysical Research Letters*, *40*, 5377–5381. https://doi.org/10.1002/2013GL057930

Secco, R. A. (2017). Thermal conductivity and Seebeck coefficient of Fe and Fe-Si alloys: Implications for variable Lorenz number. *Physics of the Earth and Planetary Interiors*, *265*, 23–34.

Silber, R. E., Secco, R. A., Yong, W., & Littleton, J. A. H. (2018). Electrical resistivity of liquid Fe to 12 GPa: Implications for heat flow in cores of terrestrial bodies. *Scientific Reports*, *8*(1), 10758.

Sotin, C., & Labrosse, S. (1999). Three-dimensional thermal convection in an iso-viscous, infinite Prandtl number fluid heated from within and from below: Applications to the transfer of heat through planetary mantles. *Physics of the earth and planetary interiors*, *112*(3), 171–190.

Tachinami, C., Senshu, H., & Ida, S. (2011). Thermal evolution and lifetime of intrinsic magnetic fields of super-Earths in habitable zones. *The Astrophysical Journal*, *726*(2), 70.

Wagle, F., Steinle-Neumann, G., & de Koker, N. (2018). Saturation and negative temperature coefficient of electrical resistivity in liquid iron-sulfur alloys at high densities from first-principles calculations. *Physical Review B*, *97*(9), 94307.

Williams, Q. (2018). The thermal conductivity of Earth's core: A key geophysical parameter's constraints and uncertainties. *Annual Review of Earth and Planetary Sciences*, *46*(1), 47–66.

Xu, J., Zhang, P., Haule, K., Minar, J., Wimmer, S., Ebert, H., & Cohen, R. E. (2018). Thermal conductivity and electrical resistivity of solid iron at earth's core conditions from first principles. *Physical Review Letters*, *121*, 96601.

Yadav, R. K., Gastine, T., Christensen, U. R., & Duarte, L. D. V. (2013). Consistent scaling laws in anelastic spherical shell dynamos. *The Astrophysical Journal*, *774*(1), 6.

Supplement to:

Geodynamo Conductivity Limits

Driscoll, P. E.[1] and Du, Z.[2,3]

[1]Department of Terrestrial Magnetism, Carnegie Institution for Science, Washington, D.C.

[2]Geophysical Laboratory, Carnegie Institution for Science, Washington, D.C.

[3]State Key Laboratory of Isotope Geochemistry, Guangzhou Institute of Geochemistry, Chinese Academy of Sciences, 510640 Guangzhou, China

June 21, 2019

Geophysical Research Letters

Changes from previous version in **bold**.

S1 Reduced Rayleigh number

The reduced Rayleigh number in (5) can be written in terms of the standard non-dimensional dynamo parameters as (Aubert et al., 2009)

$$Ra_Q = \left(\frac{r_o}{D}\right)^2 \frac{E^3(1-1/Nu)}{Pr^2} Ra \tag{S1}$$

where $E = \nu/\Omega D^2$ is the Ekman number, Ω is angular velocity of rotation, $Nu = (r_o/D)^2(qD/k\Delta T)$ is the Nusselt number, $Pr = \nu/\kappa$ is the Prandtl number, and $Ra = \alpha g q D^4/k\kappa\nu$ is the Rayleigh number (Olson and Christensen, 2006).

S2 Core cooling models

To compute the CMB heat flow we adopt the critical thermal boundary layer model from Driscoll and Bercovici (2014). According to this model the Rayleigh number at the top of the thermal boundary layer

$$Ra_{LM}(\delta_{LM}) = \frac{\alpha_{T,LM} g_{LM} \Delta T_{LM} \delta_{LM}^3}{\kappa_{LM}\nu_{LM}} \tag{S2}$$

is equal to the critical value for convection $Ra_{crit} \approx 660$ (e.g. Turcotte and Schubert, 2014), implying the boundary layer thickness is

$$\delta_{LM} = \left(\frac{Ra_{crit}\kappa_{LM}\nu_{LM}}{\alpha_{T,LM} g_{LM} \Delta T_{LM}}\right)^{1/3} \tag{S3}$$

where subscript LM refers to the lower mantle, $\alpha_{T,LM}$ is thermal expansivity, g_{LM} is gravity, $\kappa_{LM} = k_{LM}/\rho_{LM}c_m$ is thermal diffusivity, c_m is mantle specific heat, and ν_{LM} is viscosity (Driscoll and Bercovici, 2014). We note that although Ra_{crit} may differ from this ideal value due to complex rheological and compositional effects (e.g. Davaille and Limare, 2015), the value of Ra_{crit} is arbitrary here because it is only used to calibrate the reference viscosity for a chosen present day CMB heat flow Q^*_{cmb} (see (S5)).

For lower mantle viscosity ν_{LM} in (11) we adopt an Arrhenius law,

$$\nu_{LM} = \nu_r \exp\left[\frac{A_\nu}{R_g \overline{T}_{LM}}\right] \tag{S4}$$

where $\overline{T}_{LM}$ is the average of T_{LM} and T_{cmb}, A_ν is activation energy, and R_g is the gas constant. The reference viscosity is calibrated for a choice of present-day CMB heat flow by

$$\nu_r = \nu^*_{LM} / \exp\left[\frac{A_\nu}{R_g \overline{T}^*_{LM}}\right] \quad . \tag{S5}$$

Adopting a present-day CMB heat flow $Q^*_{cmb} = 12$ TW equations (S3-S5) give $\nu_r = 1.41\times10^{13}$ m^2 s^{-1}, $\nu^*_{LM} = 9.32 \times 10^{17}$ m^2 s^{-1}, and $\delta^*_{LM} = 190$ km.

Here we compare two ways to estimate ΔT_{LM}: (i) assume only the core is cooling, and (ii) assume the mantle and core secular heat loss rates are equal. In case (i) only the core is cooling and the lower mantle temperature is assumed to be constant at its present-day value $T^*_{LM} = 2500$ K, where the * implies present-day value. In case (ii) the core and mantle are

assumed to lose secular heat at the same rate

$$M_m c_m \dot{T}_m = M_c c_c \dot{T}_c \tag{S6}$$

from which equation (12) is derived. A comparison of cooling models (i) and (ii) shows they give similar results for Q_{cmb} over a wide range of T_{cmb}, deviating at most by 1.5 TW (Figure S1). In the manuscript we use cooling model (ii) where the mantle and core secular heat loss rates are equal as in (S6). Note that when the inner core nucleates the additional latent heat source will slow the core secular cooling rate, which could be modeled by adopting a larger c_c.

S3 Derivation of $Rm(\sigma, T)$

Here we derive the magnetic Reynolds number Rm in (16) by combining (1)-(11). Using (5) in (4) gives the fluid velocity u as

$$u = Ro_0 \Omega^{1-3\alpha} D^{1-4\alpha} r_o^{2\alpha} F^{\alpha} \tag{S7}$$

and using (S7) in (1) gives

$$Rm = \mu_0 Ro_0 \sigma \Omega^{1-3\alpha} D^{2-4\alpha} r_o^{2\alpha} F^{\alpha}. \tag{S8}$$

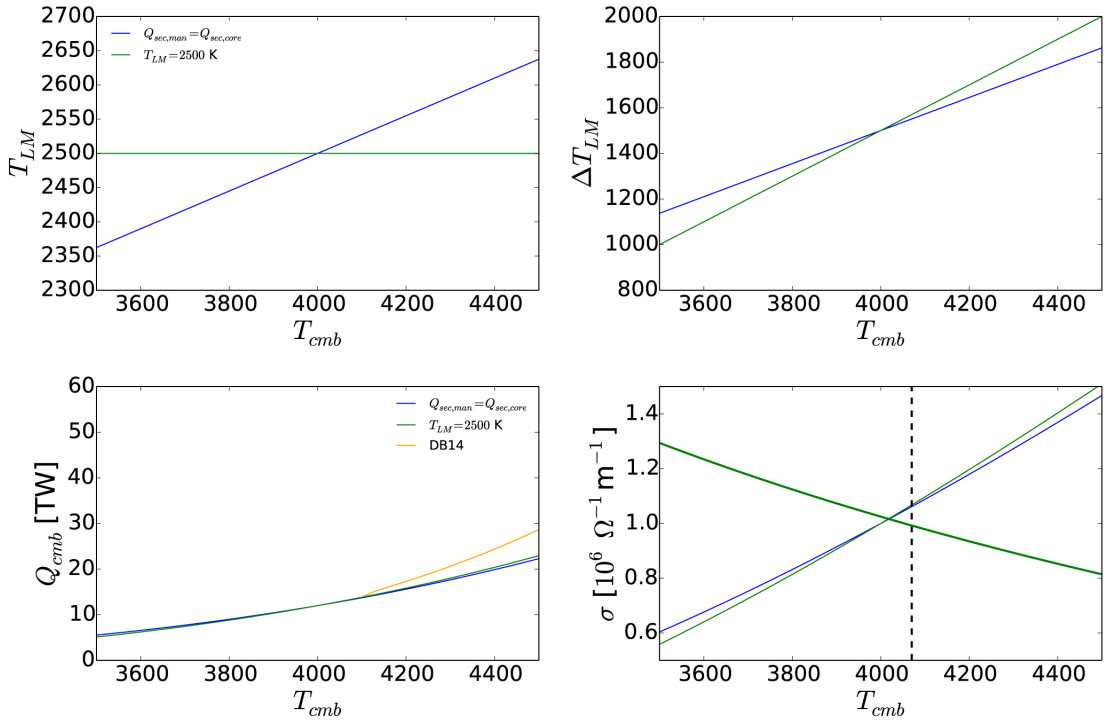

Figure S1: Comparison of core cooling models with $Q^*_{cmb} = 12$ TW. A: Lower mantle temperature T_{LM} as a function of T_{cmb} from (15). B: Same as (A) but for ΔT_{LM}. C: CMB heat flow $Q_{cmb} = A_{cmb} q_{cmb}$ from (8). Also shown is $Q_{cmb}(T_{cmb})$ from the E model of DB14 (Driscoll and Bercovici, 2014). D: Electrical conductivity σ_{crit} and σ_T vs T_{cmb} as in Figure 4. Vertical dashed line correponds to the CMB temperature when the inner core nucleates T_{icb}.

It is apparent from (S8) that Rm has roots when $\sigma = 0$ and $F = 0$. For thermal convection we write $F = F_T$ in terms of σ by using (7) in (6),

$$F_T = \frac{\alpha_{T,c} g_c}{\rho_c c_c} (q_{cmb} - q_{a,c}) \tag{S9}$$

and using the expressions for q_{cmb} and $q_{a,c}$ in (8) and (9) in (S9),

$$F_T = \frac{\alpha_{T,c} g_c}{\rho_c c_c} \left[k_{LM}^{2/3} \Delta T_{LM}^{4/3} \left(\frac{\alpha_{T,LM} g_{LM} \rho_{LM} c_m}{Ra_c \nu_{LM}} \right)^{1/3} - \sigma L \gamma_{a,c} T_{cmb}^2 \right] \tag{S10}$$

which can be rearranged to

$$F_T = \frac{\alpha_{T,c} g_c L \gamma_{a,c}}{\rho_c c_c} \sigma T_{cmb}^2 \left[\frac{\sigma_{crit}}{\sigma} - 1 \right] \tag{S11}$$

where the root σ_{crit} is defined in (18). Finally, using (S11) in (S8) gives $Rm(\sigma, T)$ in (16).

S4 Derivation of dynamo electrical conductivity limits

To derive the electrical conductivity limits where the magnetic Reynolds number is at the critical value for dynamo action we set $Rm = Rm_D = 40$ in (16) and solve for σ_D. We consider the two limits separately because (16) is transcendental in σ_D. At the lower limit where $\sigma = \sigma_{D1}$, $\sigma_{crit}/\sigma >> 1$ so we can use the approximation

$$\{\sigma_{crit}/\sigma - 1\}^{\alpha} \approx \{\sigma_{crit}/\sigma\}^{\alpha} \tag{S12}$$

and solve for σ_{D1} in (16), which is shown in (19). At the upper limit where $\sigma = \sigma_{D2}$, Rm is dominated by the term in brackets so we approximate the first σ-term in (16) as $\sigma^{1+\alpha} \approx \sigma_{crit}^{1+\alpha}$ and solve for σ_{D2} in (16), which is shown in (20).

S5 General form of Rm

The expression for Rm in (16) can be generalized to the form,

$$f = x^{\alpha+1}\left\{x^{-\beta}-1\right\}^{\alpha} \tag{S13}$$

where the variables have been scaled as $x = \sigma/\sigma_2$ and $f = Rm\sigma_2^{\alpha+1}/(Rm_0 T_{cmb}^{2\alpha})$. There are two possible values of β. In application to the core where both the mantle and core conductivities are relevant (and different) the exponent is $\beta = 1$. In a case where a single thermal conductivity controls both heat loss and conduction this exponent becomes $\beta = 1/3$. The roots of (S13) are $x_1 = 0$ and $x_2 = 1$, and has a peak at

$$x_3 = \left[1 - \frac{\beta}{1+1/\alpha}\right]^{1/\beta} . \tag{S14}$$

The general form in (S13) is shown in Figure S2 for two values of β and α. Interestingly the peak value of f is higher for $\beta = 1$ than $\beta = 1/3$, implying that dynamos overlain by an electrical and thermal insulators (such as Earth's mantle) will tend to produce stronger magnetic fields. f differs by $\sim$7% between the Coriolis-inertia-buoyancy balance with $\alpha = 2/5$ (Christensen and Aubert, 2006) and Coriolis-Lorentz-buoyancy balance with $\alpha = 4/9$ (Davidson, 2013).

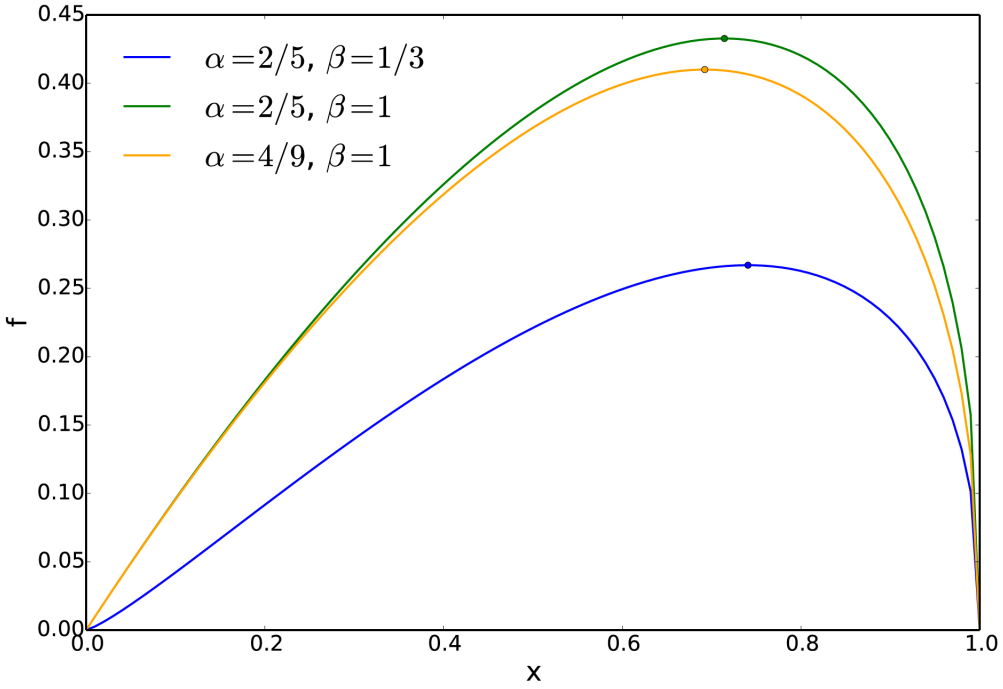

Figure S2: General form f from (S13) for $\beta = 1/3$ or $\beta = 1$ and $\alpha = 2/5$ or $\alpha = 4/9$.

S6 Temperature-dependent electrical conductivity

In Figure 4 we show the temperature-dependent electrical conductivity of Earth's core $\sigma(T) = 1/\rho$, where ρ is resistivity,

$$\rho = f_{melt}(\rho_{Fe}^{-1} + \rho_{Le}^{-1})^{-1} \tag{S15}$$

where ρ_{Fe} and ρ_{Le} are the pure iron contribution to and light element depression of the resistivity, respectively, and $f_{melt} = 1.2$ is the increase in resistivity upon melting Ohta et al.

(2016). The pure iron conductivity is approximated by

$$\rho_{Fe} = 1.7 \times 10^{-7} + 1.05 \times 10^{-10}(T_{cmb} - 1520) \tag{S16}$$

and light element depression by

$$\rho_{le} = (f_{melt}/86.9 \times 10^{-8} - 1/40.4 \times 10^{-8})^{-1} \tag{S17}$$

where the coefficients are from Ohta et al. (2016). For $T_{cmb} = 4000$ K equations (S15-S17) give $\rho = 97.5$ $\mu\Omega$ cm and $\sigma = 1.02 \times 10^6$ Ω^{-1} m^{-1}.

Parameter	Value	Definition	Reference
A_ν	3×10^5 J mol^{-1}	Activation energy	DB14
$\alpha_{T,LM}$	1×10^{-5} K^{-1}	Lower mantle thermal expansivity	DB14
$\alpha_{T,c}$	1.35×10^{-5} K^{-1}	Core thermal expansivity	D15
c_m	1260 J kg^{-1} K^{-1}	Mantle specific heat	DB14
c_c	715 J kg^{-1} K^{-1}	Core specific heat	D15
g_{LM}, g_{cmb}	10.68 m s^{-2}	Lower mantle, CMB gravity	DB14
Γ	~ 0.275	Ratio of core to mantle heat capacity	Section 2
k_{LM}	10 W m^{-1} K^{-1}	Lower mantle thermal conductivity	O12
L_0	2.44×10^{-8} WΩK^{-2}	Ideal Lorentz number	P17
ν_r	1.41×10^{13} m^2 s^{-1}	Viscosity coefficient	Section 3
Ra_{crit}	660	Critical Rayleigh number	TS14
ρ_{LM}	4418 kg m^{-3}	Lower mantle density	DB14
ρ_c	9903 kg m^{-3}	Core density	DB14
σ^*	1×10^6 Ω^{-1} m^{-1}	Core electrical conductivity	O16
T^*_{cmb}	4000 K	Present-day CMB temperature	DB14
T^*_{LM}	2500 K	Present-day lower mantle temperature	DB14

Table S1: Constants used in the calculations. Reference abbreviation DB14 is Driscoll and Bercovici (2014), D15 is Davies (2015), O12 is Ohta et al. (2012), O16 is Ohta et al. (2016), P17 is Pourovskii et al. (2017), and TS14 is Turcotte and Schubert (2014).

References

Aubert, J., Labrosse, S., Poitou, C., 2009. Modeling the paleo-evolution of the geodynamo. Geophys. J. Int. 179 (3), 1414–1428, doi: 10.1111/j.1365–246X.2009.04361.x.

Christensen, U., Aubert, J., 2006. Scaling properties of convection-driven dynamos in rotating spherical shells and application to planetary magnetic fields. Geophys. J. Int. 166 (1), 97–114, doi: 10.1111/j.1365–246X.2006.03009.x.

Davaille, A., Limare, A., 2015. 7.03 - Laboratory studies of mantle convection. In: Schubert, G. (Ed.), Treatise on Geophysics (Second Edition), second edition Edition. Elsevier, pp. 73–144.

Davidson, P. A., 06 2013. Scaling laws for planetary dynamos. Geophysical Journal International 195 (1), 67–74.

Davies, C. J., 2015. Cooling history of Earths core with high thermal conductivity. Physics of the Earth and Planetary Interiors 247, 65–79.

Driscoll, P., Bercovici, D., 2014. On the thermal and magnetic histories of Earth and Venus: Influences of melting, radioactivity, and conductivity. Physics of the Earth and Planetary Interiors 236, 36–51.

Ohta, K., Kuwayama, Y., Hirose, K., Shimizu, K., Ohishi, Y., 2016. Experimental determination of the electrical resistivity of iron at Earths core conditions. Nature 534 (7605), 95–98.

Ohta, K., Yagi, T., Taketoshi, N., Hirose, K., Komabayashi, T., Baba, T., Ohishi, Y., Hernlund, J., 2012. Lattice thermal conductivity of MgSiO3 perovskite and post-perovskite at the core–mantle boundary. Earth and Planetary Science Letters 349, 109–115.

Olson, P., Christensen, U., 2006. Dipole moment scaling for convection-driven planetary dynamos. Earth Planet. Sci. Lett. 250 (3-4), 561–571.

Pourovskii, L. V., Mravlje, J., Georges, A., Simak, S. I., Abrikosov, I. A., Jul 2017. Electron–electron scattering and thermal conductivity of -iron at Earth's core conditions. New Journal of Physics 19 (7), 073022.

Turcotte, D., Schubert, G., 2014. Geodynamics. Cambridge university press.